Scientific Research Publishing

Open Journal of Applied Sciences, 2026, 16(4), 1049-1067
https://www.scirp.org/journal/ojapps
ISSN Online: 2165-3925
ISSN Print: 2165-3917

Physics-Informed LSTM for Fatigue Life Prediction of Rubber Isolators under Thermo-Mechanical Coupling

Shen Liu, Fei Meng*

School of Management, University of Shanghai for Science and Technology, Shanghai, China
Email: *feimeng@usst.edu.cn

How to cite this paper: Liu, S. and Meng, F. (2026) Physics-Informed LSTM for Fatigue Life Prediction of Rubber Isolators under Thermo-Mechanical Coupling. *Open Journal of Applied Sciences*, **16**, 1049-1067.
https://doi.org/10.4236/ojapps.2026.164062

Received: March 6, 2026
Accepted: April 4, 2026
Published: April 7, 2026

Abstract

Rubber supports are ubiquitous in modern vibration isolation systems. Their fatigue evolution under coupled thermo-mechanical loading is exceptionally complex. Traditional life prediction methods rely heavily on empirical formulas. These methods often lack accuracy and extrapolation capabilities under varying temperatures. To address this, we propose a novel LSTM-PINN architecture. This framework integrates physical constitutive relations and temperature effects into a neural network. We used transfer learning to extract baseline physical data across wide temperature ranges. Long Short-Term Memory (LSTM) layers capture sequential loading features. We embedded partial differential equations (PDEs) into the loss function. These PDEs are based on strain energy density (SED) and Arrhenius thermodynamics. This approach ensures strict adherence to physical laws. Results demonstrate that LSTM-PINN achieves high precision even with small datasets. It also exhibits superior out-of-distribution (OOD) generalization. This framework provides a new paradigm for evaluating the reliability of rubber components.

Keywords

Rubber Isolator, Fatigue Life, PINN, LSTM, Thermo-Mechanical Coupling

1. Introduction

Rubber supports are essential in automotive, heavy machinery, and aerospace engineering. They offer excellent hyper elasticity, viscoelastic dissipation, and noise reduction [1]-[3]. In service, these components face high-frequency cyclic loads and fluctuating temperatures. Such harsh conditions cause microscopic cross-link damage and thermal aging. This degradation leads to significant macroscopic

stiffness loss. Consequently, service reliability and NVH (noise, vibration, and harshness) performance decline [4]. Accurately predicting fatigue under multi-physical coupling is therefore critical. Traditional rubber fatigue assessment often adapts frameworks used for metals. These include nominal stress or local strain methods. However, rubber exhibits significant geometric and material nonlinearity. Its fatigue failure shows high spatial and temporal complexity.

Standard S-N curves cannot accurately map load, temperature, and damage rates. This limitation restricts their generalization across different operating conditions [5]. Furthermore, fatigue testing is expensive and time-consuming. High-quality data is often scarce, limiting purely data-driven models.

Artificial Neural Networks (ANNs) have recently emerged as powerful tools [6]. Convolutional Neural Networks (CNNs) outperform traditional regression for fatigue prediction [7] [8]. However, these models require massive destructive experimental datasets [9]-[12]. Under "small-sample" constraints, data-driven models often lack physical interpretability. They are also prone to overfitting [13].

Physics-Informed Neural Networks (PINNs) offer a promising alternative [14]. PINNs embed governing physical equations (PDEs) into the network's loss function [15]. This forces the model to follow physical laws while fitting data. This characteristic ensures robustness when dealing with limited experimental samples. Initially, PINNs were applied primarily to metals and additive manufacturing. For instance, Wang *et al.* integrated micro-defect features into PINNs [14]. Other researchers incorporated stress-strain relations and crack growth equations [16] [17]. These studies confirmed that physical constraints reduce data dependency [18] [19].

However, applying PINNs to natural rubber (NR) is still in its infancy. Rubber fatigue is more complex than metal fatigue. It involves large deformations, viscoelasticity, and thermo-mechanical damage. Current rubber predictions still rely on empirical models [20] [21]. A deep learning framework that captures both temporal evolution and thermodynamics is missing.

Rubber isolators endure complex, time-varying random loads during service. LSTM networks are excellent at capturing long-range temporal dependencies. In metal fatigue studies, Zhao *et al.* improved LSTM accuracy using attention mechanisms [22]. LSTM-based methods are also widely used for battery and bearing health monitoring. Yet, pure LSTM models lack inherent physical constraints. They risk physical inconsistency when modeling rubber's nonlinear stiffness decay. Their generalization in multi-condition, small-sample scenarios is often poor.

Recently, hybrid PINN frameworks combining LSTM or GRU have gained interest. Sharma *et al.* used GRU-PINN for battery temperature prediction [23]. Tang *et al.* embedded heat transfer mechanisms into LSTMs [24]. These hybrids effectively capture nonlinear temporal constraints [25].

This paper proposes a novel LSTM-PINN hybrid architecture. First, we use transfer learning to extract temperature-dependent physical baselines. Second, the LSTM layer extracts features from cyclic loads. Finally, we embed damage evolution PDEs into the loss function. These PDEs are based on SED and Arrhenius

thermodynamic mechanisms. This ensures consistency between physical laws and engineering priors. The framework improves accuracy and OOD generalization under extreme data constraints. This study offers a high-efficiency paradigm for rubber fatigue assessment.

The paper is organized as follows: Section 2 describes the LSTM-PINN architecture. Section 3 details the experimental setup and data augmentation. Section 4 compares the predictive performance across various temperatures. Section 5 summarizes the main findings.

2. Methodology

2.1. Fatigue Failure Criterion

There is no unified standard for fatigue failure criteria of rubber materials. Previous studies have used static stiffness degradation as a key indicator of fatigue damage [26]. Literature [27] reports that rubber materials exhibit significant static stiffness reduction after fatigue loading. According to the TB/T 2843 standard, the tolerance limits for static property changes of rubber elastic components after fatigue are ±20% for strict tolerance and ±30% for normal tolerance. Based on the service requirements of actual vehicle suspension structures and engineering experience, this study adopts a 25% reduction in static stiffness as the fatigue failure criterion, which is expressed by the following formula:

$$\Delta K = \frac{K_0 - K_f}{K_0} \times 100\% \tag{1}$$

Where, ΔK represents the static stiffness degradation rate, K_0 is the initial static stiffness, and K_f is the static stiffness after fatigue.

2.2. Long Short-Term Memory (LSTM)

Stiffness decay in rubber isolators is a characteristic sequential process. Current stiffness depends on both present loads and the history of damage. Therefore, we selected Long Short-Term Memory (LSTM) as the baseline prediction model. LSTM employ a unique gating mechanism to process sequential data effectively [28]. The architecture coordinates input, forget, and output gates to manage information flow. Recurrent connections enable the transfer of information across multiple stages. These gating units precisely regulate the internal state of the network. This specific design mitigates gradient vanishing and explosion during long-sequence training. Consequently, LSTMs are the preferred architecture for processing complex sequential features.

LSTMs excel at capturing the temporal dynamics of rubber stiffness decay. Fatigue involves cumulative damage under cyclic loading. This process mirrors the long-term dependencies found in sequential data. **Figure 1** illustrates the typical structure of an LSTM memory cell. It depicts the interaction between input, forget, and output gates. This mechanism enables selective information retention during sequence processing. In this study, the LSTM inputs include cycle number

N, initial stiffness, ambient temperature T, and strain amplitude ε. The model outputs the predicted static stiffness S(N).

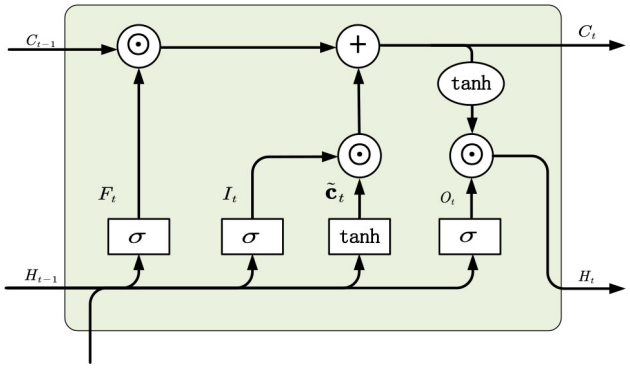

Figure 1. A cell of LSTM.

A standard LSTM unit contains three key gating structures. These gates use sigmoid activation functions to control information flow. This allows the model to selectively retain or discard historical data. The forget gate $\boldsymbol{f}_t$ determines how much information to discard from the previous state $\boldsymbol{c}_{t-1}$.The input gate I_t decides which new information $\boldsymbol{c}_t$ enters the current cell state. The output gate $\boldsymbol{o}_t$ produces the hidden state $\boldsymbol{h}_t$ based on the updated cell state $\boldsymbol{c}_t$. The core mathematical expressions for these gates are as follows:

$$\boldsymbol{f}_t = \sigma\left(\boldsymbol{W}_f \cdot \left[\boldsymbol{h}_{t-1}, \boldsymbol{x}_t\right] + \boldsymbol{b}_f\right) \tag{2}$$

$$I_t = \sigma\left(\boldsymbol{W}_i \cdot \left[\boldsymbol{h}_{t-1}, \boldsymbol{x}_t\right] + \boldsymbol{b}_i\right) \tag{3}$$

$$\tilde{\boldsymbol{c}}_t = \tan h\left(\boldsymbol{W}_c \cdot \left[\boldsymbol{h}_{t-1}, \boldsymbol{x}_t\right] + \boldsymbol{b}_c\right) \tag{4}$$

$$\boldsymbol{c}_t = \boldsymbol{f}_t \odot \boldsymbol{c}_{t-1} + \boldsymbol{i}_t \odot \tilde{\boldsymbol{c}}_t \tag{5}$$

$$\boldsymbol{o}_t = \sigma\left(\boldsymbol{W}_o \cdot \left[\boldsymbol{h}_{t-1}, \boldsymbol{x}_t\right] + \boldsymbol{b}_o\right) \tag{6}$$

$$\boldsymbol{h}_t = \boldsymbol{o}_t \odot \tan h\left(\boldsymbol{c}_t\right) \tag{7}$$

Where, σ represents the sigmoid function. tanh is the hyperbolic tangent function. The symbol ⊙ denotes element-wise multiplication. W and b represent weight matrices and bias vectors, respectively.

2.3. The LSTM-PINN Framework

Traditional fatigue prediction methods often lack extrapolation power and suffer from data sparsity. To overcome these challenges, we propose a hybrid LSTM-PINN model. This architecture integrates the sequential processing of LSTMs with the physical constraints of PINNs.

The model ensures that predictions fit experimental data while strictly obeying mechanical laws. As shown in Figure 2, the model uses four primary inputs: initial baseline stiffness, number of cycles (N), strain amplitude (ε) and ambient temperature (T). The model outputs the predicted stiffness decay curve. To explicitly de-

termine the fatigue life, the predicted curve is continuously evaluated until the stiffness S(N) drops below the 25% degradation threshold ($0.75\times K_0$) established in our failure criterion, at which point the corresponding cycle number N is recorded as the predicted fatigue life N_f . This hybrid approach leverages LSTMs to capture temporal dependencies. Simultaneously, the PINN component enforces physical consistency via the loss function. This dual mechanism significantly improves generalization under varying temperatures.

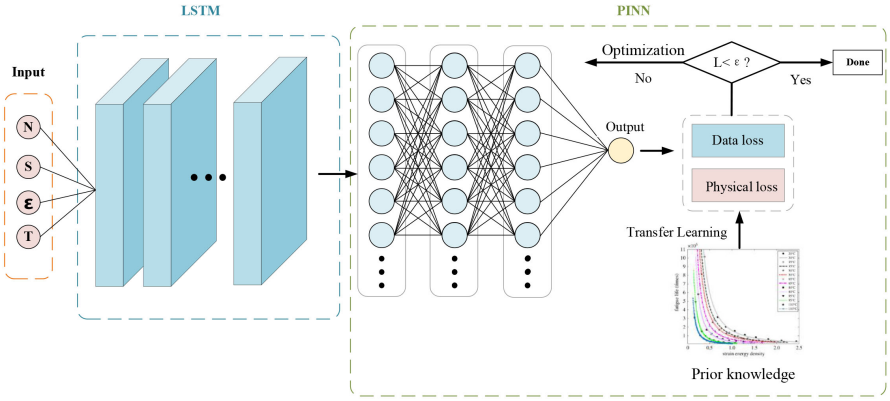

Figure 2. Overall architecture of the proposed LSTM-PINN constrained by thermo-mechanical-damage coupled partial differential equations (PDEs).

The core of the LSTM-PINN is treating physical knowledge as an intrinsic constraint. Rubber is a hyperplastic material with highly nonlinear stress-strain behavior. We employ the Yeoh model to describe this relationship accurately. The Yeoh model is a polynomial constitutive framework. It is ideal for describing the large-strain behavior of polymers. For isotropic and incompressible rubber, the initial strain energy density (W) is defined as:

$$W_0\left(I_1,T\right)=\sum_{i=1}^{3}C_i\left(T\right)\left(I_1-3\right)^i \tag{8}$$

Where, I_1 is the first principal strain invariant, and C_i represents the material constants. To embed thermodynamic prior knowledge into the neural network, baseline Yeoh constitutive parameters were extracted from literature databases for Nitrile Butadiene Rubber (NBR) across a wide temperature range (20˚C to 110˚C) [29]. The specific parameter values are detailed in **Table 1**.

Table 1. Parameters of Yeoh model under different temperature conditions.

Temperature (˚C)	C_1 (MPa)	C_2 (MPa)	C_3 (MPa)
35	0.9098	0.001724	0.00498
50	0.8602	0.01799	0.00112
80	0.6752	−0.00092	0.00188
95	0.5106	−0.0059	0.00223
110	0.4576	−0.00599	0.00262

Because both the source domain literature data and our target engine mount utilize NBR-based elastomers, their thermo-rheological degradation manifolds exhibit strong physical homology. Rather than employing a disjointed step-by-step training strategy, the LSTM-PINN framework incorporates these parameters as initial thermodynamic constraints. During the joint training process, the network adaptively fine-tunes these priors via backpropagation driven directly by the target domain data. This unified optimization ensures the parameter space seamlessly shifts to match the specific properties of the target isolator while preserving the physically grounded temperature trends learned from the source domain. The loss function for this stage is defined as follows:

$$L_{prior} = \frac{1}{M}\sum_{j=1}^{M}\sum_{i=1}^{3}\left\|\hat{C}_{i,pred}\left(T_j\right) - C_{i,source}\left(T_j\right)\right\|^2 \tag{9}$$

Fatigue fundamentally involves the continuous destruction of internal microstructures, such as polymer cross-link networks. We therefore introduce a continuum damage variable, D. The material remains intact when $D = 0$. Macroscopic failure occurs when D reaches a critical threshold, D_c. We apply the effective stress equivalence hypothesis. Consequently, the partial differential constitutive relationship between damaged strain energy density and nominal stress is modified as follows:

$$\frac{\partial W}{\partial \varepsilon} = \left(1 - D(N)\right)\cdot 2\left(\lambda - \lambda^{-2}\right)\sum_{i=1}^{3} i \cdot C_i(T)\left(I_1 - 3\right)^{i-1} \tag{10}$$

The formula (10) represents stress as the gradient of strain energy density with respect to strain. It defines the constitutive relationship of the hyperplastic material. This equation serves as a physics layer within the PINN architecture. It ensures that predicted stress-strain states strictly adhere to continuum mechanics principles.

Strain energy density (SED) is the primary energy source driving damage. It is defined as the integral area under the stress-strain curve for a single cycle. Our theoretical framework avoids explicit numerical integration. Instead, the network calculates the SED directly using analytical formulas through the physics layer:

$$\omega = W\left(\varepsilon_{\max}\right) = \sum_{i=1}^{3} C_i(T)\left(I_{1,\max} - 3\right)^i \tag{11}$$

Based on energy dissipation theory and Miner's rule, the damage increment $\frac{\partial D}{\partial N}$ follows a power-law relationship with strain energy density W. Temperature T significantly accelerates molecular chain scission via thermal activation effects. We integrated a modified Arrhenius equation to construct the following partial differential equation for damage evolution:

$$\frac{\partial D}{\partial N} = \left[k_0 \exp\left(\frac{E_a}{R}\left(\frac{1}{T_0} - \frac{1}{T}\right)\right)\right]^{-1}\cdot \omega^{-b} \tag{12}$$

The decay of macroscopic static stiffness S(N) manifests internal damage D(N).

Differentiating both sides with respect to N yields a governing PDE. This equation directly constrains the neural network output:

$$\frac{\partial S}{\partial N} = -S_0 \cdot \left[k_0 \exp\left(\frac{E_a}{R}\left(\frac{1}{T_0} - \frac{1}{T} \right) \right) \right]^{-1} \cdot \omega^{-b} \tag{13}$$

Where E_a denotes the apparent activation energy. R represents the universal gas constant, fixed at 8.314 J/(mol·K). S_0 signifies the initial baseline stiffness extracted from experimental data. We define S_0 as the static stiffness after 1000 cycles. This ensures the Mullins effect softening has stabilized before measurement. k_0 is the room-temperature fatigue baseline factor. We do not obtain these parameters through traditional log-linear fitting. Instead, we initialize them as trainable tensors within the deep learning framework. During training, the network optimizes these values autonomously via gradient descent. This process relies on the backpropagation of physical PDE residuals.

The engineering boundary condition loss L_{bc} ensures consistent failure definitions. We established Dirichlet boundary conditions for the system based on the criterion in Section 2.1:

$$L_{bc} = \left\| \hat{S}_{pred}\left(N_f \right) - 0.75 S_0 \right\|^2 \tag{14}$$

This term penalizes the discrepancy between the network's predicted slope and the derivative derived from continuum damage mechanics:

$$L_{pde} = \frac{1}{M}\sum_{j=1}^{M} \left\| \frac{\partial \hat{S}_{pred}}{\partial N} - \left(-S_0 \cdot \left[k_0 \exp\left(\frac{E_a}{R}\left(\frac{1}{T_0} - \frac{1}{T} \right) \right) \right]^{-1} \cdot \omega^{-b} \right) \right\|^2 \tag{15}$$

We formulate the LSTM-PINN training process as a multi-objective optimization problem. The total loss function comprises data-driven components and physical regularization terms:

$$L_{total} = \lambda_{data} L_{data} + \lambda_{pde} L_{pde} + \lambda_{prior} L_{prior} + \lambda_{bc} L_{bc} \tag{16}$$

The framework utilizes dynamic adaptive weights for these components. During training, the neural network automatically tunes the weight parameter λ.

3. Experiment Set-Up

3.1. Experimental Setup

This research focuses on a rubber engine mount from a passenger car. The experimental apparatus utilizes a high-performance MTS-793 electro-hydraulic servo system.

As shown in **Figure 3**, hydraulic actuators apply vertical cyclic loads to the specimen. This system ensures precise regulation of the loading waveform, frequency, and amplitude. Load cells and high-frequency displacement transducers monitor force and deformation in real-time. These instruments facilitate robust closed-loop feedback control.

Figure 3. Uniaxial fatigue test rig for elastic support specimen.

Figure 4. Air-heating/Air-cooling temperature control system.

Considering the complex thermal environment of an actual powertrain compartment, the rig features a custom heating/air-cooling system (Figure 4). Surface-mounted thermocouples monitor the rubber component's core temperature in real-time. This temperature control system maintains a constant preset temperature throughout the fatigue cycles. It effectively suppresses temperature drift caused by internal high-frequency heat generation. This ensures the experimental data remains thermally consistent and physically interpretable.

Figure 5. The attachment of strain gauges for strain measurement.

Meanwhile, strain gauges are attached to critical stress nodes to collect deformation data (Figure 5). The experiment applies continuous cyclic loading based on three typical road-load profiles. The experimental matrix involved three distinct cyclic load profiles: −6 KN - 36 KN, −8 KN - 36 KN, and 0 - 36 KN. Physical fatigue tests were conducted at elevated temperatures of 80˚C, 90˚C, and 110˚C. For each specific temperature and load combination, two independent specimens were tested. To precisely capture the degradation trajectory, the high-frequency dynamic loading was paused every 5,000 cycles to measure the macroscopic static stiffness.

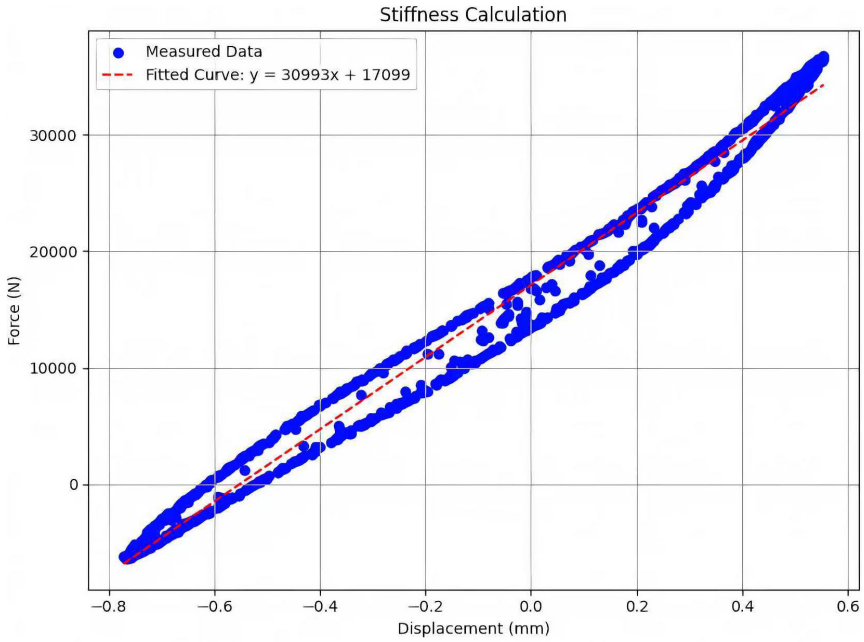

Figure 6. Stiffness measurement.

At preset fatigue cycle intervals, the system pauses the high-frequency dynamic loading. The rig then applies low-speed, small-amplitude quasi-static compression while maintaining a stable specimen temperature. We record the resulting force-displacement hysteresis loops (Figure 6). We perform linear regression on the loading-phase data using the least-squares method. The slope of this regression line defines the macroscopic static stiffness at that cycle node. This measurement protocol successfully records the typical initial Mullins softening effect. It also accurately captures the progressive physical damage features as the cycle number N increases.

3.2. FEA Data Augmentation and Validation

The generalization of the LSTM-PINN framework depends heavily on training data coverage. However, rubber fatigue experiments are costly and time-consuming. Experimental data alone cannot support the full convergence of deep networks. To overcome data scarcity, we established a parameterized virtual environ-

ment using Finite Element Analysis (FEA). We calibrated the simulation model using limited experimental data. This model then generated large-scale, multi-condition augmented datasets. These datasets provide a rich foundation for training the physics-informed neural network.

The augmentation workflow was structured based on temperature conditions: Purely Simulated Conditions (20˚C and 50˚C): Conducting long-term physical fatigue tests at lower operating temperatures is excessively time-consuming. Therefore, the stiffness degradation trajectories for the 20˚C and 50˚C conditions were generated entirely through the high-fidelity FEA simulation. For each of the three load profiles at these temperatures, three independent sets of stiffness decay data were simulated. The virtual sampling rate was set to match the physical experiment, extracting a stiffness value every 5,000 cycles. Hybrid Data Conditions (80˚C, 90˚C and 110˚C): For the higher temperature conditions, the dataset consists of a hybrid of physical and virtual samples. Physical experiments provided two actual specimen trajectories per load profile. To maintain a balanced dataset, the FEA model was utilized to generate one additional augmented trajectory per profile. This ensured a uniform dataset structure comprising exactly three sets of stiffness degradation data for every training condition.

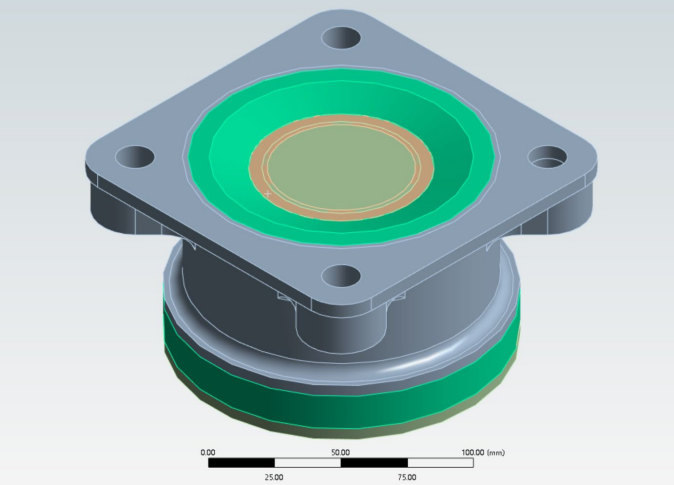

Figure 7. The finite element model of the elastic support structure.

We performed finite element calculations using ANSYS software. The three-dimensional FEA model was constructed within ANSYS Workbench. **Figure 7** displays the 3D model of the elastic support. The support structure comprises two main parts: metal components and a rubber elastomer. The rubber is injected into the metal interior via vulcanization. During operation, the rubber elastomer absorbs vibrational stress through deformation. The metal parts experience minimal stress and are treated as rigid bodies. We made three primary assumptions for the FEA model: 1. All parts except the rubber are considered rigid bodies. 2. Vibrational loads transferred through the aluminum housing remain constant and uniform. 3. Minor geometric nonlinear contacts are neglected.

We employ the Yeoh model to accurately simulate the nonlinear stress-strain behavior of the rubber. This model is particularly effective for capturing the large-strain characteristics typical of rubber-like materials. Its governing equation is given by Formula (8), where W represents the strain energy density. The variable I_1 is the first principal strain invariant. Under uniaxial tension, its relationship with the principal stretch ratio λ is defined as $I_1 = \lambda^2 + 2/\lambda$. The material constants C_i are determined by fitting experimental data. They reflect the material's initial shear modulus and hardening characteristics. These parameters capture both the linear and nonlinear responses of the rubber. Traditional methods C_i require extensive uniaxial tension tests at every target temperature T. However, the thermo-rheological properties of rubber share underlying physical similarities. Therefore, we extracted scatter data for similar base rubbers across a wide temperature range from literature databases $C_i(T)$.

The high-fidelity FEA model must be validated for thermodynamic response accuracy across a wide temperature range. This ensures it can handle large-scale data augmentation tasks. We conducted static stiffness decay tests by heating the support from 20˚C to 110˚C. Initial specimens were placed in an environmental chamber for continuous heating. We performed quasi-static compression tests every 30 minutes to record changes in mechanical properties. This process captured the material variations caused by thermal penetration. A transient thermal-mechanical coupling step was established in the FEA model. We applied thermal boundary conditions based on the measured ambient temperature curve. This simulated the transient heat diffusion from the housing to the rubber core. Simultaneously, we mapped the Yeoh constitutive parameters to local temperature distributions. Simulated stiffness values were extracted at the corresponding 30-minute intervals for comparison.

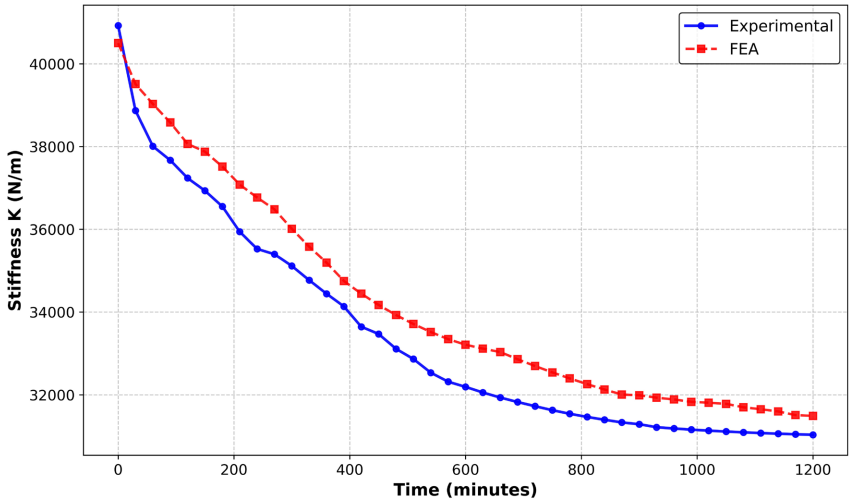

Figure 8. Comparison of experimental and FEA-simulated static stiffness degradation of the elastic mount during heating.

As shown in Figure 8, the static stiffness significantly drops from 40,924 N/mm

to 31,033 N/mm during heating. This demonstrates distinct nonlinear thermal softening characteristics. The simulation accurately captures the rapid softening at the early heating stage. It also tracks the stable transition phase after 600 minutes. The Mean Absolute Percentage Error (MAPE) is only 2.28%. This indicates the model accurately represents modulus degradation during 20 hours of transient heat conduction. The maximum relative error is 3.89%, occurring during the mid-heating phase. This minor deviation likely stems from environmental temperature fluctuations versus idealized FEA boundary conditions. However, errors under 4% meet accuracy requirements for complex thermo-mechanical engineering simulations. Comparative analysis confirms that the high-fidelity FEA model replicates the mechanical response evolution during transient heating. It matches experimental macro-stiffness and successfully couples time, temperature, and material softening.

Consequently, this model provides high-quality, cross-temperature labeled data for the LSTM-PINN framework. This compensates for the lack of physical fatigue test samples under extreme operating conditions.

4. Results and Discussion

This chapter validates the performance of the proposed LSTM-PINN framework for rubber isolator fatigue life prediction. The analysis includes training configurations and fitting accuracy across various temperature conditions. We also verify physical extrapolation performance under an unseen high-temperature condition (110˚C). Comparisons with pure data-driven LSTM models highlight the value of physical constraints in nonlinear damage evolution. All machine learning models were implemented within the TensorFlow framework using a workstation equipped with an Intel Core i9-10900X CPU, 128 GB RAM, and an NVIDIA GeForce RTX 3060 Ti GPU. The LSTM architecture was designed with 2 hidden layers, each containing 64 hidden units, and utilized a sequence length of 20 to capture long-term temporal dependencies. The unified network was optimized end-to-end using the Adam optimizer with an initial learning rate of 0.001, a batch size of 32, and a maximum of 1600 training epochs. To coordinate the multi-objective loss function efficiently, the SoftAdapt algorithm was implemented. This dynamic weighting strategy automatically updates the adaptive weight parameter λ at each epoch, continuously balancing the gradient contributions between the data-driven mean squared error (MSE) and the physical PDE residuals.

The dataset was rigorously partitioned to prevent information leakage and ensure objective evaluation. The training set incorporated the purely FEA-generated data at 20˚C and 50˚C, alongside a calibrated mixture of experimental and augmented data at 80˚C and 90˚C. To prevent data leakage, augmented data derived from a specific specimen's history were strictly prohibited from appearing in the validation set used for that same specimen. A designated subset of the 80˚C and 90˚C measurements was isolated purely for validation and hyperparameter tuning. Crucially, the 110˚C experimental dataset was strictly excluded from all stages of model fitting,

weight updating, and FEA calibration, serving exclusively as an unseen ground-truth reference for out-of-distribution (OOD) extrapolation testing.

4.1. Comparison of Fitting Accuracy at Room and Medium Temperatures

This section evaluates the model's ability to capture damage paths within known temperature fields, specifically at 20˚C and 80˚C.

At 20˚C (Figure 9), the rubber displays high initial stiffness. A sharp "steep drop" occurs early in the loading process. This is primarily attributed to the microscopic Mullins effect and initial molecular chain reorganization. The pure data-driven LSTM model exhibits significant "prediction drift" before 200,000 cycles. Its linear prediction fails to capture the curvature transition from rapid early softening to stable mid-term damage. Conversely, the LSTM-PINN model enforces non-linear energy dissipation laws via strain energy density (SED) constraints. Its trajectory aligns closely with actual measurements, perfectly replicating the gradual decay between 400,000 and 800,000 cycles. This proves that physical information effectively corrects random errors in black-box time-series forecasting.

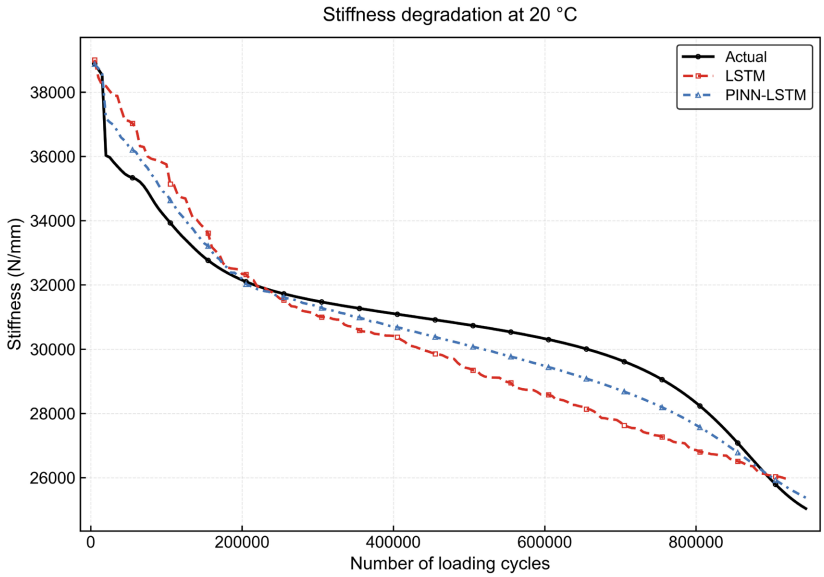

Figure 9. Comparison of stiffness evolution predictions between pure LSTM and LSTM-PINN models under interpolation at 20˚C.

At 80˚C (Figure 10), the initial stiffness drops to approximately 31,600 N/mm. This softening matches the thermal trends predicted by the Arrhenius equation. Thermal aging accelerates the nonlinear characteristics of the stiffness decay curve. The standard LSTM's performance worsens at 80˚C, deviating sharply from the ground truth after only 100,000 cycles. It even produces physically unrealistic curvature reversals near the end of life. In contrast, the LSTM-PINN utilizes fine-tuned Yeoh parameters to accurately capture physical inflection points. Even in

data-sparse regions, the model maintains high fidelity by adhering to the derivative constraints of the evolution equations.

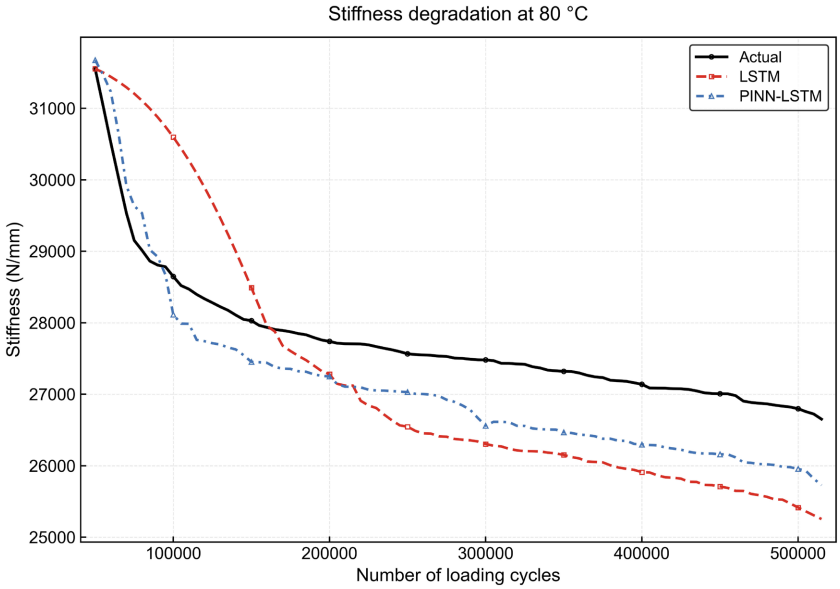

Figure 10. Comparison of stiffness evolution predictions between pure LSTM and LSTM-PINN models under interpolation at 80˚C.

4.2. Verification of Extrapolation Performance under High Temperature

Extrapolation capability is the "litmus test" for any PINN model. This section evaluates the model's generalization performance in a "knowledge blind spot" by setting an extreme temperature of 110˚C, which was not included in the training set.

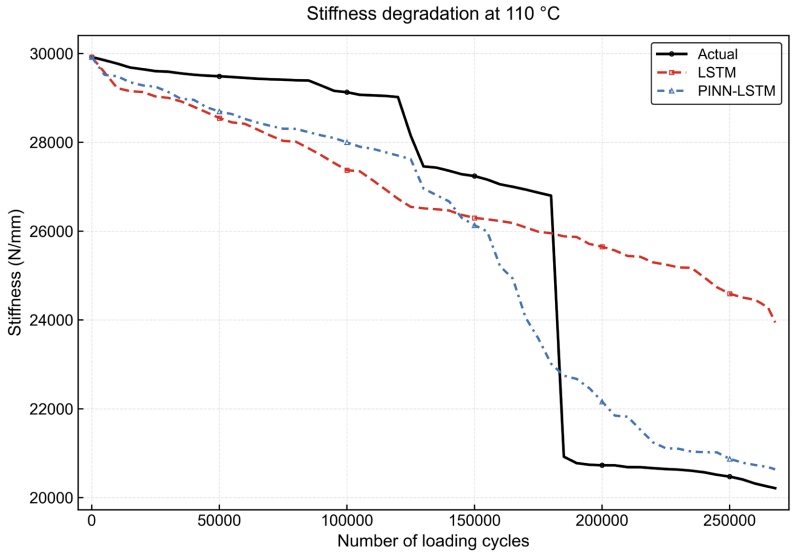

Figure 11. Comparison of stiffness evolution predictions between pure LSTM and LSTM-PINN models under physical extrapolation at 110˚C.

As shown in Figure 11, in the 110˚C extrapolation experiment, the rubber component exhibits a failure mode entirely different from those at low or medium temperatures. As the cycle count approaches 180,000, the stiffness curve shows a nearly vertical, fracture-like plunge. This signifies large-scale physical rupture or structural instability within the material.

The pure LSTM model fails completely under this condition. Having never encountered such a violent performance mutation, it produces an extremely conservative and erroneous "linear prediction". In contrast, the LSTM-PINN accurately captures the accelerated decay trend between 150,000 and 200,000 cycles.

4.3. Quantitative Analysis of Prediction Accuracy and Generalization Error

To further evaluate the performance of LSTM and LSTM-PINN, RMSE and the coefficient of determination (R^2) are used as metrics for assessing prediction accuracy. Their calculation formulas are given as follows:

$$RMSE = \sqrt{\frac{1}{n}\sum_{i=1}^{n}\left(y_{ture}^{(i)} - y_{pred}^{(i)}\right)^2} \tag{17}$$

$$R^2 = 1 - \frac{\sum_{i=1}^{n}\left(y_{ture}^{(i)} - y_{pred}^{(i)}\right)^2}{\sum_{i=1}^{n}\left(y_{ture}^{(i)} - y_{ture}\right)^2} \tag{18}$$

Where n is the number of samples; $y_{ture}^{(i)}$ is the true stiffness of the i -th sample; $y_{pred}^{(i)}$ is the stiffness predicted by the model for the i -th sample; and y_{ture} is the mean of the true values.

Table 2. Estimation results of LSTM and LSTM-PINN on different datasets (%).

Model	LSTM		LSTM-PINN	
Index	RMSE	R^2	RMSE	R^2
20˚C	1234.96	0.771	616.44	0.943
80˚C	1209.19	−0.898	702.46	0.459
110˚C	2767.17	0.501	1230.09	0.901

As shown in Table 2, at room temperature, the RMSE of the LSTM-PINN is only 616.44. This represents a reduction of approximately 50% compared to the pure LSTM. The R^2 value improved from 0.77 to 0.94. These results indicate that physical constraints enable the model to capture the nonlinear initial fatigue softening more accurately. This effectively eliminates the "prediction lag" commonly observed in pure data-driven models. At 80˚C, the R^2 of the pure LSTM dropped to a negative value (−0.898). The standard LSTM proved extremely sluggish in responding to rapid stiffness drops. Although the LSTM-PINN faced challenges from the complex damage evolution at this temperature, its R^2 returned to a positive range with significantly reduced error. This demonstrates that physical for-

mulas act as a "forced calibration" mechanism when data quality is poor. Under the extrapolated 110˚C condition, the RMSE of the standard LSTM surged to 2767.17, indicating a massive prediction failure. In contrast, the LSTM-PINN maintained a much lower RMSE of 1230.09. Beyond stiffness metrics, when evaluating the ultimate fatigue life prediction—defined by the cycle count where stiffness reaches the 25% loss threshold—the LSTM-PINN achieved an average life-prediction error of only 8.4% under the 110˚C extrapolation condition. This significantly outperforms the pure data-driven LSTM model, which yielded a catastrophic life-prediction error of 62.1%. These results confirm that lacking physical logic leads to pure data models suffering from severe "hallucination" in unobserved temperature domains.

These results provide strong evidence that when temperatures exceed the training range, pure data-driven models suffer from "hallucination" due to a lack of physical logic. However, the LSTM-PINN—leveraging its embedded thermodynamic evolution equations—continues to predict stiffness decay paths that strictly adhere to physical laws.

5. Conclusions

This research addresses the challenge of predicting the fatigue life of rubber isolators under thermo-mechanical-damage coupling. We developed an LSTM-PINN framework that integrates prior physical knowledge transfer with Partial Differential Equation (PDE) constraints. Through experimental validation, FEA data augmentation, and multi-condition analysis, we have achieved the following results:

(1) This paper establishes a novel paradigm by utilizing high-fidelity Finite Element Analysis (FEA) for data augmentation. This approach effectively compensates for the long cycles and data scarcity inherent in fatigue testing. By calibrating the model with limited experimental "ground truth" and covering wide-range scenarios via large-scale simulation, physical equations provide a global constraint. This represents an efficient path for the digital twin development and reliability assessment of polymer materials. This paradigm enhances prediction efficiency and provides theoretical support for the health monitoring of elastic components in complex service environments.

(2) We have moved beyond the traditional "black-box" paradigm by designing an LSTM-PINN topology with synergistic constitutive and evolution branches. Through transfer learning, prior knowledge of Yeoh model moduli is injected directly into the network's parameter space, solving the "cold start" problem. By constructing a unified objective function containing both data-driven and physical residual losses, the model automatically balances gradients between physical laws and experimental data. This ensures predictions adhere to the energy dissipation criteria of Continuum Damage Mechanics (CDM) while fitting observed trends.

(3) Quantitative evaluation shows that within known temperature ranges, the

LSTM-PINN significantly outperforms standard LSTM models. The physical constraints successfully correct prediction paths, ensuring stiffness evolution matches the fundamental logic of thermal softening. In unseen extreme high-temperature extrapolation, pure LSTM models fail due to a lack of physical logic. In contrast, the LSTM-PINN demonstrates robust generalization. This proves the model captures the underlying thermo-mechanical damage manifold rather than mere statistical correlations. This provides a reliable algorithmic foundation for the health monitoring of isolators in varying temperature environments.

Conflicts of Interest

The authors declare no conflicts of interest regarding the publication of this paper.

References

[1] Yao, Q., Dong, P., Zhao, Z., Li, Z., Wei, T., Wu, J., *et al.* (2023) Temperature Dependent Tensile Fracture Strength Model of Rubber Materials Based on Mooney-Rivlin Model. *Engineering Fracture Mechanics*, **292**, Article ID: 109646. https://doi.org/10.1016/j.engfracmech.2023.109646

[2] Liu, X., Zhao, X. and Liu, X. (2022) A Unified Probabilistic Fatigue Life Prediction Model for Natural Rubber Components Considering Strain Ratio Effect. *Fatigue & Fracture of Engineering Materials & Structures*, **46**, 1473-1487. https://doi.org/10.1111/ffe.13941

[3] Cheng, Z., Wang, H. and Wang, P. (2022) A Multi-Grid Sampling Multi-Scale Method for Crack Initiation and Propagation. *Engineering Fracture Mechanics*, **271**, Article ID: 108671. https://doi.org/10.1016/j.engfracmech.2022.108671

[4] Chong, Z., Yue, T., Yao, Q., Li, X., Zheng, C., Xia, Z., *et al.* (2021) Experimental and Numerical Investigation of Crack Propagation in Bolting Systems Strengthened with Resin-Encapsulated Rock Bolts. *Engineering Failure Analysis*, **122**, Article ID: 105259. https://doi.org/10.1016/j.engfailanal.2021.105259

[5] Wang, X., Sedaghati, R., Rakheja, S. and Shangguan, W. (2025) Rubber Fatigue Revisited: A State-of-the-Art Review Expanding on Prior Works by Tee, Mars and Fatemi. *Polymers*, **17**, Article No. 918. https://doi.org/10.3390/polym17070918

[6] Sun, Y., Liu, X., Yang, Q., Liu, X. and He, K. (2024) Improving Fatigue Life Prediction of Natural Rubber Using a Physics-informed Neural Network Model. *Fatigue & Fracture of Engineering Materials & Structures*, **48**, 1039-1049. https://doi.org/10.1111/ffe.14533

[7] Liu, X. and Wang, X. (2022) Natural Rubber Components Fatigue Life Estimation through an Extreme Learning Machine. *Proceedings of the Institution of Mechanical Engineers, Part L: Journal of Materials: Design and Applications*, **237**, 81-91. https://doi.org/10.1177/14644207221102567

[8] Liu, X., Zhao, X. and Shangguan, W. (2022) Fatigue Life Prediction of Natural Rubber Components Using an Artificial Neural Network. *Fatigue & Fracture of Engineering Materials & Structures*, **45**, 1678-1689. https://doi.org/10.1111/ffe.13690

[9] Hottin, A., Naït Abdelaziz, M., Talha, A. and Charrier, P. (2023) Continuum Damage Mechanics to Predict Rubber Fatigue Life under Multiaxial Loadings. *International Journal of Fatigue*, **170**, Article ID: 107559. https://doi.org/10.1016/j.ijfatigue.2023.107559

[10] Pan, Z., Lai, Y., Wang, Y., Duan, W., Qiao, Y., Liu, Y., *et al.* (2021) Fatigue Life Prediction and Effects of Cerium Oxide-Filled Vulcanized Natural Rubber on Fatigue Life under Multiaxial Loading. *Fatigue & Fracture of Engineering Materials & Structures*, **44**, 3349-3362. https://doi.org/10.1111/ffe.13561

[11] Tavosi, S., Alimardani, M., Ghoreishy, M.H.R. and Tavakol, M. (2024) Fatigue Failure Modeling in Rubber Stator of Downhole Motors: Dependency to Materials and Geometry, and Its Application to Life Prediction. *Engineering Failure Analysis*, **159**, Article ID: 108072. https://doi.org/10.1016/j.engfailanal.2024.108072

[12] Robin, E., Le Cam, J., Delahaye, G., Ruellan, B., Di Cesare, N. and Canévet, F. (2025) A First Proposal for Fatigue Life Prediction of Carbon Black Filled Natural Rubber at Different Temperatures with an Artificial Neural Network. *Strain*, **61**, e70001. https://doi.org/10.1111/str.70001

[13] Bang, J., Choi, M., Lee, H., Jeong, S., Yoon, J. and Doh, J. (2025) Data-Efficient and Uncertainty-Aware RUL Prediction Using Physics-Informed Neural Networks: Application to Degraded Rubber Components. *Annual Conference of the PHM Society*, **17**. https://doi.org/10.36001/phmconf.2025.v17i1.4356

[14] Wang, L., Zhu, S., Luo, C., Niu, X. and He, J. (2023) Defect Driven Physics-Informed Neural Network Framework for Fatigue Life Prediction of Additively Manufactured Materials. *Philosophical Transactions of the Royal Society A: Mathematical, Physical and Engineering Sciences*, **381**. https://doi.org/10.1098/rsta.2022.0386

[15] Chen, J. and Liu, Y. (2022) Fatigue Modeling Using Neural Networks: A Comprehensive Review. *Fatigue & Fracture of Engineering Materials & Structures*, **45**, 945-979. https://doi.org/10.1111/ffe.13640

[16] Halamka, J., Bartošák, M. and Španiel, M. (2023) Using Hybrid Physics-Informed Neural Networks to Predict Lifetime under Multiaxial Fatigue Loading. *Engineering Fracture Mechanics*, **289**, Article ID: 109351. https://doi.org/10.1016/j.engfracmech.2023.109351

[17] Wang, H., Li, B., Gong, J. and Xuan, F. (2023) Machine Learning-Based Fatigue Life Prediction of Metal Materials: Perspectives of Physics-Informed and Data-Driven Hybrid Methods. *Engineering Fracture Mechanics*, **284**, Article ID: 109242. https://doi.org/10.1016/j.engfracmech.2023.109242

[18] Chen, D., Li, Y., Liu, K. and Li, Y. (2023) A Physics-Informed Neural Network Approach to Fatigue Life Prediction Using Small Quantity of Samples. *International Journal of Fatigue*, **166**, Article ID: 107270. https://doi.org/10.1016/j.ijfatigue.2022.107270

[19] Dong, Y., Yang, X., Chang, D. and Li, Q. (2025) Predicting Fatigue Life of Multi-Defect Materials Using the Fracture Mechanics-Based Physics-Informed Neural Network Framework. *International Journal of Fatigue*, **190**, Article ID: 108626. https://doi.org/10.1016/j.ijfatigue.2024.108626

[20] Li, Z., Dai, W., Yue, H., Guo, C., Ji, Z., Li, Q., *et al.* (2025) Fatigue Life Prediction of 2024-T3 Clad Al Alloy Based on an Improved SWT Equation and Machine Learning. *Materials*, **18**, Article No. 332. https://doi.org/10.3390/ma18020332

[21] Keqi Luo, R. (2024) Fatigue Prediction Criteria for Rubber Antivibration Design with Temperature Effects. *International Journal of Fatigue*, **183**, Article ID: 108271. https://doi.org/10.1016/j.ijfatigue.2024.108271

[22] Liu, Z., Meng, X., Wei, H., Chen, L., Lu, B., Wang, Z., *et al.* (2021) A Regularized LSTM Method for Predicting Remaining Useful Life of Rolling Bearings. *International Journal of Automation and Computing*, **18**, 581-593. https://doi.org/10.1007/s11633-020-1276-6

[23] Sharma, M., Samanta, A. and Williamson, S. (2025) Integrating Physics-Informed Neural Networks and GRU for SciML-Based Surface Temperature Prediction Li-Ion Battery. 2025 *IEEE Energy Conversion Congress & Exposition Asia* (*ECCE-Asia*), Bengaluru, 11-14 May 2025, 1-6. https://doi.org/10.1109/ecce-asia63110.2025.11112113

[24] Tang, X., Hong, Q., Liu, Y., Wang, B., Cui, Z. and Shao, W. (2025) Physics-Informed LSTM Based Dynamic Model of Heat Exchanger and Application on the Thermal Management System Considering Time Delay. *International Journal of Heat and Mass Transfer*, **250**, Article ID: 127322. https://doi.org/10.1016/j.ijheatmasstransfer.2025.127322

[25] Khanra, S., Kukreja, V.K. and Bala, I. (2025) Forecasting India's Demographic Transition under Fertility Policy Scenarios Using Hybrid LSTM-PINN Model.

[26] Zhang, Z., Zhou, Y. and Vassiliou, M.F. (2023) Experimental, Numerical, and Theoretical Studies on Vertical Stiffness Reduction of Lead Thick Rubber Bearings. *Construction and Building Materials*, **384**, Article ID: 131421. https://doi.org/10.1016/j.conbuildmat.2023.131421

[27] Zhou, Y., Zhang, Z. and Vassiliou, M.F. (2022) Investigation on Vertical Stiffness Reduction of Thick Rubber Bearings under Lateral Displacement. *Construction and Building Materials*, **360**, Article ID: 129563. https://doi.org/10.1016/j.conbuildmat.2022.129563

[28] Al-Selwi, S.M., Hassan, M.F., Abdulkadir, S.J., Muneer, A., Sumiea, E.H., Alqushaibi, A., *et al.* (2024) RNN-LSTM: From Applications to Modeling Techniques and Beyond—Systematic Review. *Journal of King Saud University—Computer and Information Sciences*, **36**, Article ID: 102068. https://doi.org/10.1016/j.jksuci.2024.102068

[29] Zhang, J., Xue, F., Wang, Y., Zhang, X. and Han, S. (2018) Strain Energy-Based Rubber Fatigue Life Prediction under the Influence of Temperature. *Royal Society Open Science*, **5**, Article ID: 180951. https://doi.org/10.1098/rsos.180951